Differential Triple Coils for Rail-bottom Flaw Detection Using Single-cycle Demodulation

Yong Li,[1,2] Liyun Ou,[1] Na Li,[1*] and Zhe Tan[1]

[1]Public Security Department, Fujian Police College,
Fuzhou, Fujian 350007, China
[2]College of Computer and Data Science/College of Software, Fuzhou University,
Fuzhou, Fujian 350108, China

To meet the requirements of rail-bottom flaw detection, we use a differential-triple-coil sensor at low frequencies to detect rail-bottom flaws. Aiming at its online application to railways, we propose a single-cycle demodulation algorithm. To increase the ability to remove multiple interference signals in an electromagnetic environment, we analyze the anti-interference performance of the proposed algorithm in the frequency domain. We also discuss a method of achieving high anti-noise performance in rail-bottom flaw detection. In addition, we form artificial horizontal rail-bottom flaws in a standard rail specimen and carry out experiments on four horizontal rail-bottom flaws with different depths using the embedded inspection system. The experimental results demonstrate that the differential-triple-coil sensor with the proposed single-cycle demodulation algorithm can be used for horizontal rail-bottom flaw detection. Furthermore, horizontal rail-bottom flaws with a depth of less than 7 mm can be detected.

1. Introduction

The railway is the artery of China's national economy, playing a major role in improving people's livelihoods. As a part of the railway infrastructure, the rail is an important part of guaranteeing the safe operation of trains.[1] Owing to the direct contact with sleepers, the rail bottom is extremely easily corroded. During long-term service, the pressure from wheels aggravates the corrosion of the rail bottom, generating various types of defects and even causing fracture of the rail.[2] According to the data obtained from annual inspections of the railway, two-thirds of major safety accidents were caused by broken rails, with lateral defects of the rail bottom being the main factor. Therefore, such lateral defects are a hazard in train operation, making the detection of rail-bottom defects of great significance.

The traditional technologies for rail defect detection mainly include the ultrasonic method, visual method, and eddy-current method.[1,3,4] The ultrasonic method uses echoes to determine

---

whether there is a defect. However, during ultrasonic testing, the probe and the rail must be coated with a couplant because the rough contact surface affects the accuracy of the test. In general, the ultrasonic probe is placed on a smooth tread, then high-frequency ultrasonic energy is transmitted from the tread to the inside of the rail. The energy decays with increasing depth. The ultrasonic energy returned after the energy reaches the bottom of the rail is insufficient to generate a signal with a significant amplitude, resulting in a failure to detect rail-bottom defects. Therefore, the area at the bottom corner of the rail is also a blind spot for ultrasonic flaw detection. In addition, the surface and near surface of the rail are blind regions in ultrasonic testing due to the short-distance reflection of ultrasound. In contrast, the visual method is used to detect surface defects on a rail but cannot detect subsurface or deeper defects. Thus, the subsurface or inner area of the rail is a blind area in the visual method, making it unsuitable for rail-bottom defect detection. The eddy-current method is based on the principle of electromagnetic induction. It has the advantages of no contact, no pollution, a high detection speed, and a simple setup, and it has been applied to railway sites and in other fields.[5–9] However, the eddy-current technology can only detect rail defects within 5 mm of the surface, whereas rail-bottom flaws are more than 5 mm from the surface. Although there is a skin effect in a ferromagnetic material, the detectable area inside a rail can theoretically be extended through low-frequency excitation. Therefore, to further study the eddy-current method to detect rail-bottom defects, in this paper, we propose a differential-triple-coil array to detect rail-bottom defects at different depths to verify the feasibility of defect detection at depths greater than 5 mm and to improve electromagnetic rail-bottom defect detection.

In addition, ambient or systematic noise disturbs the signal of a detection coil. In particular, at railway sites, the interference of a strong current with a frequency of 50 Hz is the greatest ambient noise, and the white noise from the circuit is the main system noise. In addition, a parasitic capacitance between the inputs of two differential coils results in measurement error. When the detected signal is amplified, the ambient and systematic noise mixed in the signal is also amplified, affecting the detection result. At present, lock-in amplification technology is widely used in weak signal detection. Because of its high signal-to-noise ratio (SNR), it is suitable for extracting the target signal at a specific frequency when the signal is superimposed with both strong noise and the multi-frequency interference, i.e., when the SNR is low.[10–12] In addition, the demodulation speed is the key to capturing the change in the signal resulting from a rail-bottom defect. Therefore, in this paper, we propose a fast single-cycle demodulation algorithm based on the principle of lock-in amplification, which can demodulate the amplitude of the signal within a sinusoidal signal cycle.

This paper is organized as follows. In Sect. 2, the principle of differential triple coils for the detection of rail-bottom defects is given in detail. Section 3 describes the single-cycle demodulation algorithm for the online application, and the frequency-domain response is also analyzed. Then, an experiment on rail-bottom defect detection using differential triple coils is designed and carried out. The experimental results are discussed and analyzed in Sect. 4. Finally, a conclusion is drawn in Sect. 5.

2.   Principle of Differential Triple Coils

Figure 1 shows a schematic diagram of the electromagnetic detection of rail-bottom defects and damage using differential triple coils. When a sinusoidal electrical signal is applied to the intermediate excitation coil, an eddy current is generated on the bottom surface of the rail. If there is damage or a defect on the bottom surface or inside of the rail, the redistribution of the surface eddy current is detected by the detection coils at both ends. Eddy currents have a skin effect on ferromagnetic materials.[13] When the penetration depth is x, the distribution of the magnetic field intensity **H** on the bottom surface of the rail can be described by[5]

$$\frac{d^2\mathbf{H}}{dx^2} = j\omega\mu\sigma\mathbf{H}. \tag{1}$$

Here, σ is the conductivity of the rail, μ is the relative permeability of the rail, and ω is the angular frequency of the excitation current. The eddy-current distribution excited on the rail surface can be obtained from

$$J = J_0 \exp(-\frac{1+j}{2}\sqrt{\omega\mu\sigma}x). \tag{2}$$

Here, J_0 represents the surface distribution of the eddy current. Then, the penetration depth of the eddy current, i.e., the skin depth, is obtained as

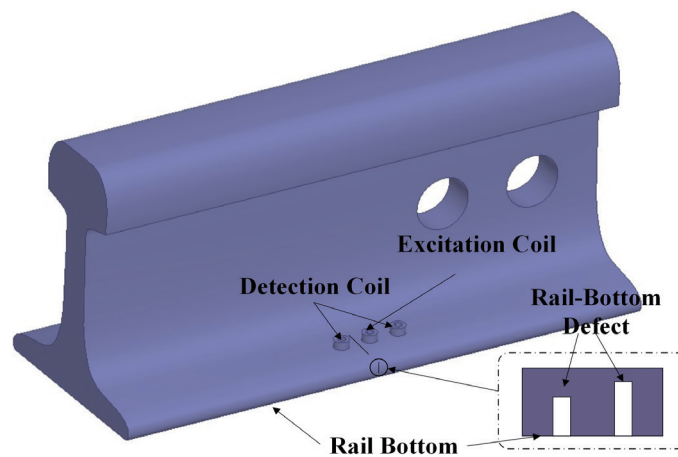$$x = \sqrt{\frac{2}{\omega\mu\sigma}}. \tag{3}$$

Fig. 1.   (Color online) Schematic diagram of differential triple coils for rail-bottom defect detection.

From Eq. (3), the penetration depth depends on the physical properties of the object to be measured and the excitation frequency. A decrease in the frequency increases the intensity of the eddy current and increases the penetration depth. Therefore, the optimal excitation frequency for the ferromagnetic object is below several hundred hertz.[5] This means that to detect rail-bottom defects, it is necessary to reduce the excitation frequency in the eddy-current detection method.

When the excitation coil is fed with a sinusoidal signal, an alternating magnetic field is excited in the space, and part of the magnetic field lines enter the detection coil through the rail, as shown in Fig. 1. Then, the magnetic field line through the detection coil generates voltage U_d on the coil, where U_d satisfies the relationship

$$U_d = f\left(B_e(x,y) \quad B_o(x,y) \quad \mu \quad \sigma(x,y)\right) \quad (x,y) \in S. \tag{4}$$

Here, B_e is the magnetic induction intensity generated by the excitation coil, B_o is the magnetic induction intensity of the detection coil, which is affected by the rail surface and internal defects of the rail, and S is the measured closed area of the rail surface. Assuming that B_e in space is a sinusoidal function of frequency and is time dependent, the magnetic field strength on the rail surface can be calculated using Maxwell's equations as follows.

$$\nabla \times \mathbf{H} = \sigma\mathbf{E} + j\omega\varepsilon\mathbf{E}, \nabla \times \mathbf{E} = -j\omega\mathbf{B}, \nabla \cdot \mathbf{B} = 0, \nabla \cdot \mathbf{D} = 0 \tag{5}$$

Here, $\mathbf{B}$ is the magnetic flux density, $\mathbf{H}$ is the magnetic field strength, $\mathbf{E}$ is the electric field strength, and $\mathbf{D}$ is the electric flux density. Because the excitation frequency is relatively small, the displacement current can be ignored, that is, $j\omega\varepsilon\mathbf{E} = 0$. Then the voltage U_d of the detection coil is obtained as

$$U_d = -n\frac{d\Psi}{dt} = -n\frac{d(\mathbf{B} \cdot \mathbf{S}_d)}{dt}. \tag{6}$$

Equation (7) is the basic mathematical model of the eddy-current method for rail-bottom defect detection. Here, Ψ is the magnetic flux through the detection coil, while n and $\mathbf{S}_d$ are the number of turns and cross-sectional area of the detection coil, respectively. The magnetic field is excited by the excitation magnetic field in space. Its magnetic induction line enters the detection coil through the surface of the rail. When there is a defect or damage on the surface or inside of the rail, the magnetic induction line, or the magnetic flux, passing through the detection coil changes with the distribution of the surface or inner defect. Furthermore, it can be seen from Eq. (6) that the damage is reflected in the voltage U_d across the detection coil when the magnetic flux changes. Because of the difference in displacement between the two detection coils, the minor changes resulting from deeper defects can be captured by monitoring the induced voltages of two such coils with the same parameters. Therefore, rail defects can be detected by measuring the voltage difference between the two ends of the detection coil ΔU_d.

3. Single-cycle Demodulation Algorithm

3.1 Single-cycle phase-locked demodulation

Let the analog signal be $S_o(t) = A\sin(2\pi f_o t + \theta)$, the reference signal be $x_R(t) = \sin(2\pi f_o t)$, and $y_R(t) = \cos(2\pi f_o t)$. Then, the representation of the sequence with sampling frequency f_s is as follows.

$$S_o[k] = A\sin\left[2\pi \times \frac{f_o}{f_s} \times k + \theta\right] \tag{7}$$

$$x_R[k] = \sin\left[2\pi \times \frac{f_o}{f_s} \times k\right] \tag{8}$$

$$y_R[k] = \cos\left[2\pi \times \frac{f_o}{f_s} \times k\right] \tag{9}$$

In Eqs. (8)–(10), $0 \leq k \leq N-1$, fo is the frequency of the target signal, A and θ are the amplitude and phase angle of the target signal, respectively, and $N = f_s/f_o$ is the number of sampling points of a full cycle. Note that the values of the reference sequence can be stored in a look-up table, reducing computational resources and time.

In accordance with the principle of phase locking, the target signal $S_o[k]$ is multiplied by the reference signals $x_R[k]$ and $y_R[k]$ to obtain the sequences $u_o[k]$ and $w_o[k]$, respectively. Next, an N-point average filter is utilized to filter the alternate current part. The direct current part is the remaining part in two such sequences.

$$X = \sum_{k}^{N} u_o[k] = \frac{1}{2} AN\cos[\theta] \tag{10}$$

$$Y = \sum_{k}^{N} w_o[k] = \frac{1}{2} AN\sin[\theta] \tag{11}$$

Finally, the amplitude and phase angle are respectively obtained as

$$A = 2\sqrt{X^2 + Y^2} \tag{12}$$

$$\theta = \arctan\frac{Y}{X}. \tag{13}$$

3.2   Frequency domain analysis

For a lock-in demodulation algorithm, a low-pass filter is very important to improve the performance. The N-point average filters in Eqs. (10) and (11) are equivalent to a time-domain rectangular window with a uniform coefficient $1/N$ for all points. The window can be described as

$$h_{LPF}[k] = \frac{1}{N}. \tag{14}$$

This window can also be seen as a time-domain window that shifts by one sampling time during one computing cycle. Therefore, we apply the discrete-time Fourier transform (DTFT) to Eq. (14) to obtain the frequency response as

$$\left| h\left(e^{j\Omega}\right) \right| = \left| \frac{\sin(N\Omega/2)}{N\sin(\Omega/2)} \right|. \tag{15}$$

Here, there are zero-crossing points at $\Omega = 2\pi k/N$, and the amplitude response of Eq. (15) is shown in Fig. 2. It can be seen that the amplitude response is reduced to zero at the zero-crossing points. In addition, the first zero-crossing point, i.e., $\Omega = 2\pi/N$, determines the ability to suppress noise or the cutoff frequency. Thus, the higher the sampling frequency, the better the performance of the quadrature demodulation algorithm because of the greater number of averaging points N.
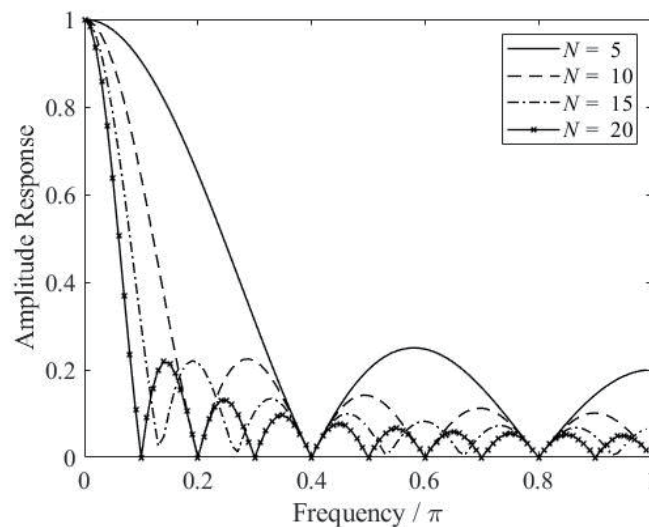

Fig. 2.   Amplitude response with different numbers of points N.

4.   Experiment and Results

4.1   Detection system for rail-bottom flaws

In reference to the design of a rail-bottom flaw detection system using electromagnetic tomography (EMT), a schematic diagram of the horizontal rail-bottom flaw detection system is shown in Fig. 3(a);[6] as can be seen, the rail-bottom flaw detection system consists of a front-end differential-triple-coil sensor, an analog amplifier board, and a signal processing unit. The arrangement of the front-end differential-triple-coil sensor is shown in Fig. 1, and the coil is made of enameled wire. Since rail-bottom flaws are detected by changes in the voltage difference between two detection coils, the parameters of the two detection coils are kept the same in theory. The parameters of each coil of the front sensor are shown in Table 1. Then, the voltage difference is amplified by the analog amplifier board and processed in the microcontroller unit (MCU). The signal processing, i.e., the single-cycle demodulation algorithm, is performed in the MCU. However, the performance of the signal processing depends on the SNR of the input analog signal. Therefore, the key to rail-bottom flaw detection is the analog amplifier board, whose physical map is shown in Fig. 3(b). As can be seen from Fig. 3(b), the input signal
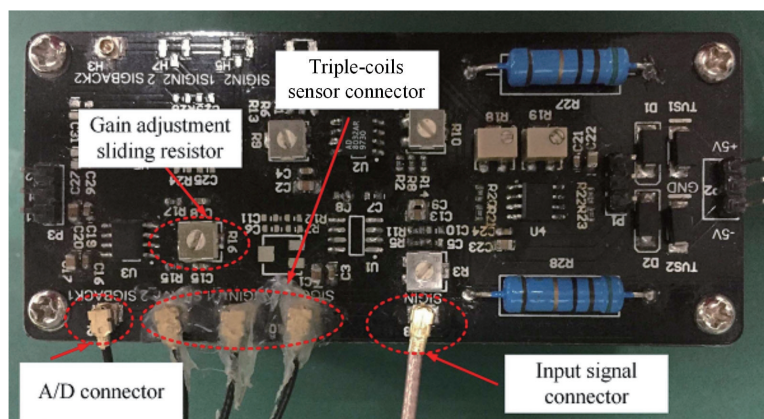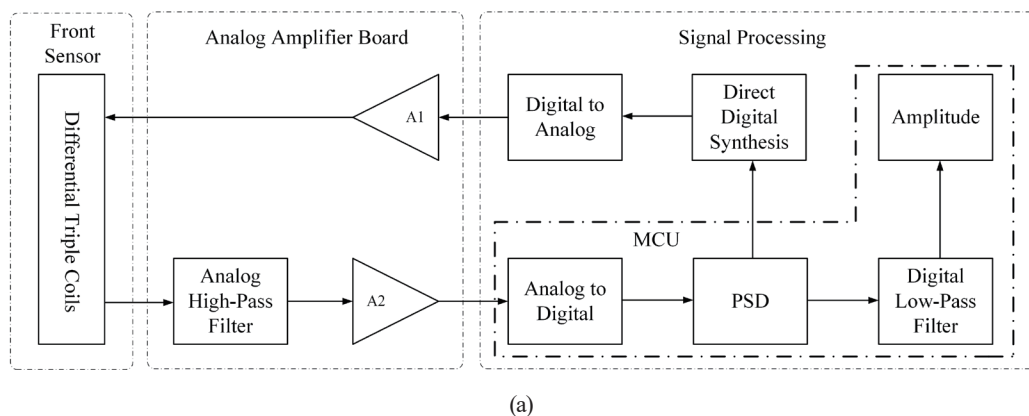

(a)

(b)

Fig. 3.   (Color online) System for rail-bottom flaw detection. (a) Schematic diagram. (b) Analog amplifier board.

Table 1
Parameters of the differential triple coils.

Gap (mm)	Type	Wire diameter (mm)	Number of turns	Outer diameter (mm)	Inner diameter (mm)	Height of coil (mm)
26	Detection 1	0.02	1000	20	10	17
26	Excitation	0.02	1000	20	10	17
26	Detection 1	0.02	1000	20	10	17

connector is used to input the sinusoidal signal into the excitation coil. The analog-to-digital (A/D) connector is connected to the A/D module built in the MCU. The triple-coil sensor connector is connected to the differential triple coils in turn. Furthermore, the amplifier gain can be adjusted by the gain adjustment sliding resistor, which is used to adjust the amplification factor of amplifier A2 in Fig. 3(a).

As discussed in Sect. 2, the defect can be found from the change in the demodulated amplitude of the differential voltage. As can be seen from Fig. 3(a), the excitation signal is generated by direct digital synthesis (DDS). The MCU is used to control the DDS to output a sinusoidal signal and set the excitation frequency by programming. Then, the excitation signal is injected into the excitation coil after being amplified by amplifier A1. According to the principle of the differential triple coils, the voltage is induced in two detection coils, and the difference voltage is amplified by amplifier A2 after passing through the analog high-pass filter. Here, the common mode rejection ratio (CMRR) is approximately 80 dB after measuring the input and output voltages. Then, the difference voltage is converted into a digital signal by the A/D module and input into the MCU. Finally, the amplitude of the difference voltage is demodulated by the single-cycle demodulation algorithm. Furthermore, the demodulated amplitude is sent to the PC through the serial port to display its change over time. According to the simulation of the single-cycle demodulation algorithm in Sect. 3.2, low-frequency excitation can effectively reduce the interference of both white noise and high-frequency signals. Moreover, the interference signals are low-frequency interference in practice. Therefore, the analog high-pass filter inside the analog amplifier board is used to reduce the low-frequency interference to increase the noise immunity of the single-cycle demodulation algorithm.

4.2 Horizontal cracks under rail bottom

To detect rail-bottom flaws, the excitation frequency is chosen as 10 kHz. According to Ohm's law, the impedance must be sufficiently large for the induced voltage to be detected; otherwise, the induced voltage is very weak. Therefore, the triple coil comprises 1000 turns of a copper wire to provide a sufficient coil impedance for the induced differential voltage to be detected. Figure 4 illustrates the experimental setup of the differential triple coils for rail-bottom flaw detection. In the experimental setup, the standard rail specimen is a heavy rail of mass 75 kg/m, and four artificial flaws in the form of transverse cracks are located at the rail bottom near the ground. The side view of the rail-bottom flaws shown in Fig. 4(a) is consistent with the schematic diagram of Fig. 1. The four rail-bottom flaws are marked in Fig. 4(b), and their dimensions are shown in Table 2. Note that the parameters in Tables 1 and 2 are defined in Fig.
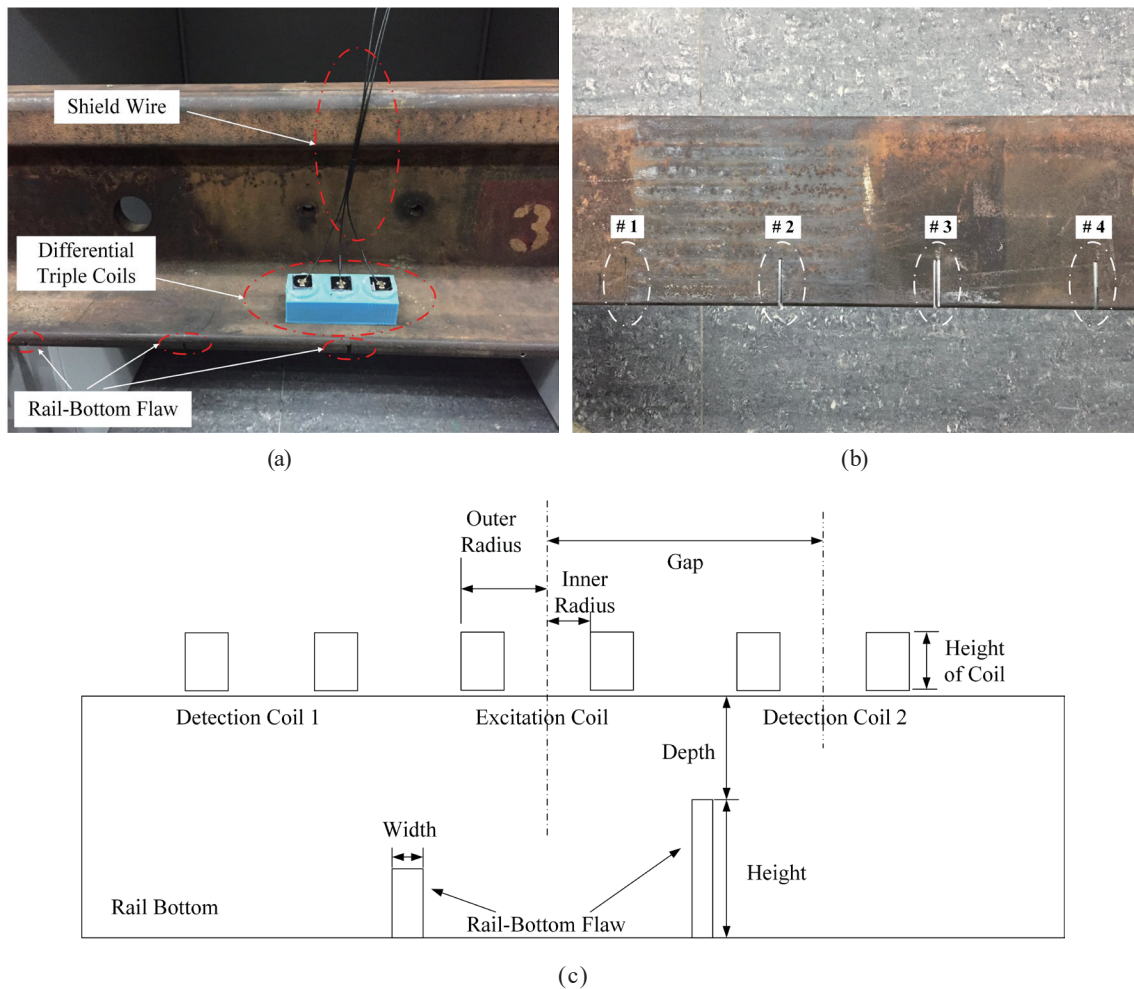
(a)

(b)

(c)

Fig. 4.   (Color online) Experimental setup. (a) Placement of front sensor. (b) Rail-bottom flaws. (c) Schematic diagram of rail-bottom flaw detection.

Table 2
Parameters of the artificial horizontal cracks of the rail bottom.

Flaw	Length (mm)	Width (mm)	Height (mm)	Depth (mm)
#1	36.5	1.5	2.0	12.0
#2	36.5	3.3	5.0	9.0
#3	36.5	3.3	7.0	7.0
#4	36.5	3.3	9.0	5.0

4(c). To avoid the overlapping effects of the four artificial flaws, the distance between the flaws is greater than 1.5 times the length of the sensor array, i.e., 108 mm. In the experiment, the differential-triple-coil sensor is placed on top of each defect and is moved over each defect by hand. After sampling the induced voltage of the differential triple coils, the single-cycle demodulation algorithm is performed in the MCU. Then, disturbances in the amplitude of the responses of the differential triple coils are captured to demonstrate the detection of the rail-bottom flaws.

As shown in Table 2, flaws #1–#4 are set to have the same lateral length, i.e., 36.5 mm. This is because the detected area covered by the lateral length of the flaw is a blind area in the ultrasonic method, which is also the main problem to be solved in this study. Here, the width, height, and depth of rail-bottom flaw #1 are set as the smallest values and used for comparison. The fabrication of a crack with a width of less than 1 mm is very difficult and costly. Thus, to reduce costs, the width of flaw #1 is 1.5 mm and that of flaws #2–#4 is 3.3 mm. In addition, the flaws have different depths to evaluate the detection of rail-bottom flaws of different depths using the differential-triple-coil sensor. Note that the depths of the flaws in Table 2 equal the value of the equivalent thickness of the rail bottom minus the height of the flaw. Because the rail is wedge-shaped, the thickness of the rail bottom decreases from the inside to the outside. Therefore, an equivalent thickness of the rail bottom must be selected for each flaw. Furthermore, the front sensor is moved along the middle of the inclined surface of the rail bottom, at which the thickness of the rail bottom is about 14 mm.

4.3   Experimental analysis

Figure 5 shows the differential voltage of the differential-triple-coil sensor used to detect the rail-bottom flaws at different depths. In the experiment, the differential-triple-coil sensor was manually moved along the direction perpendicular to each rail-bottom flaw. The front of the sensor was aligned with the adjacent side of the rail-bottom flaw, then the sensor was moved so that it passed through the entire rail-bottom flaw. Finally, the end of the sensor was aligned with the other side of the rail-bottom flaw. At the same time, the MCU controlled the built-in A/D module to sample the voltage and then demodulate its amplitude.

As shown in Fig. 5, the sampling point represents the moving time, which can be converted into the position using the moving speed. However, the speed at which the sensor was manually moved cannot be determined. Therefore, the horizontal coordinate of Fig. 5 cannot be used to definitively infer the corresponding position of the sensor. According to Sect. 2, the identification of the rail-bottom flaw is mainly based on the fluctuation of the demodulated amplitude of the differential voltage, and the precise position of the sensor is not important. Although the position of the sensor is uncertain, the time corresponding to the number of samples can be determined. That is, the sampling point can substantially represent the uncertain position of the sensor. In addition, the length of the sensor and the width of the rail-bottom flaw are also determined, and the displacement of the movement is thus determined. This means that the speed of a manually moved sensor can be judged from the number of sampling points: the fewer the sampling points, the greater the speed. In practice, the impedances of the two detection coils are not the same. However, the demodulated amplitude must maintain a stable value when the sensor passes through a position without defects, despite the different impedances of the two detection coils. The stable value fluctuates when the differential-triple-coil sensor approaches a rail-bottom flaw and returns to its previous value when the differential-triple-coil sensor completely passes through the rail-bottom flaw. Therefore, an identical impedance of the two detection coils is also not essential.
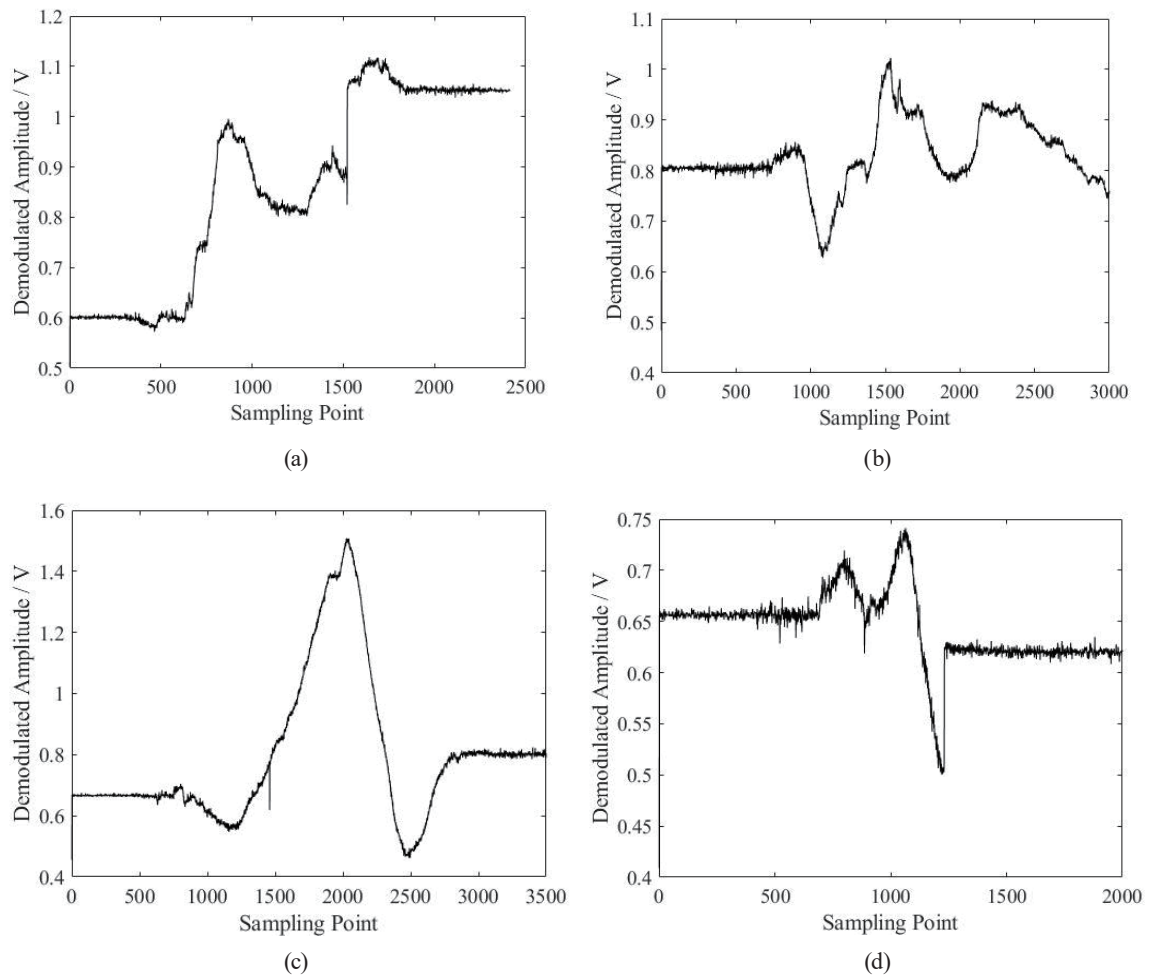
Fig. 5.   Result of demodulation in rail-bottom flaw detection. (a) Flaw #1. (b) Flaw #2. (c) Flaw #3. (d) Flaw #4.

It can be seen from Fig. 5(a) that the demodulation result of flaw #1 does not return to its value before the fluctuation caused by flaw detection by the differential-triple-coil sensor. Moreover, Fig. 5(b) demonstrates that the demodulated amplitude of flaw #2 fluctuates similarly to in Ref. 14 when the first detection coil passes through the rail-bottom flaw but decreases when the second detection coil passes through the rail-bottom flaw. In contrast to the demodulation result of flaw #2, those of flaw #3 and flaw #4 exhibit a stable amplitude when the differential-triple-coil sensor passes through the rail-bottom flaw, as shown in Figs. 5(c) and 5(d), respectively. That is, the demodulation results in Figs. 5(c) and 5(d) can be used to identify rail-bottom flaws as expected. In addition, comparing the demodulation results in Figs. 5(c) and 5(d) reveals that the maximum demodulated amplitude of flaw #4 is smaller than that of flaw #3. Theoretically, the closer the rail-bottom flaw is, the greater the fluctuation in the demodulated amplitude used for flaw detection, which means that the maximum demodulated amplitude of flaw #4 should greater than those of flaw #2 and flaw #3, but this is not the case. It can be seen from Fig. 5 that the numbers of sampling points of flaw #2 and flaw #4 are 3000 and 2000,

respectively. However, the number of sampling points of flaw #3 is 3500. This indicates that the manual movement of the sensor in the detection of rail-bottom flaw #3 is slower than that in the detection of flaw #2 and flaw #4. When the sensor rapidly moves through the rail-bottom flaw, the change in the magnetic field is difficult to capture by the MCU with a low operating frequency, which results in the maximum demodulated amplitude not being recorded even though the single-cycle demodulation algorithm is performed on the MCU. This is also the reason why the demodulation result of flaw #3 differs from the expected result. Therefore, to effectively identify the rail-bottom flaw, the differential-triple-coil sensor is preferably moved at a low speed and the operating frequency of the MCU should be high.

Therefore, it can be concluded from the above discussion that the demodulation results of flaw #1 and flaw #2 cannot be used to identify rail-bottom flaws. This means that the differential-triple-coil sensor cannot detect a rail bottom with a depth of more than 9 mm. Although the demodulation results of flaw #3 and flaw #4 are worse than expected, the differential-triple-coil sensor can detect a rail-bottom flaw at a depth of less than 7 mm. Therefore, the experiment demonstrates the feasibility of the differential-triple-coil sensor for detecting horizontal rail-bottom cracks using the single-cycle demodulation algorithm under low-frequency excitation. Moreover, a low speed of the sensor was shown to be advantageous for rail-bottom flaw detection.

5. Conclusion

We studied the application of differential-triple-coil sensors for horizontal rail-bottom flaw detection. Firstly, the detection was analyzed in principle, where the differential voltage of the differential triple coils was used to identify the rail-bottom flaw. Next, a single-cycle demodulation algorithm was proposed. It was found by numerical simulation that low-frequency excitation has better anti-noise performance. Then, to verify the feasibility of the differential-triple-coil sensor for horizontal rail-bottom flaw detection, an embedded flaw detection system was designed, and an experiment on rail-bottom flaw detection was carried out. In the experiment, four horizontal cracks with different depths were fabricated on a standard rail bottom. The experimental results demonstrated that the differential-triple-coil sensor can detect horizontal rail-bottom cracks with depths less than 7 mm. Our experiment demonstrated the feasibility of the differential-triple-coil sensor for detecting rail-bottom flaws using a single-cycle demodulation algorithm.

References

1 M. P. Papaelias, C. Roberts, and C. L. Davis: Proc. Institution of Mechanical Engineers Part F J. Rail and Rapid Transit **222** (2008) 367–384.

2   F. C. R. Hernández, G. Plascencia, and K. Koch: Eng. Failure Anal. **16** (2009) 281.
3   Y. Fan, S. Dixon, R. S. Edwards, and J. Xu: AIP Conf. Proc. **40** (2007) 1609.
4   L. Wei and C. Liang: J. Instrum. **4** (2009) 12001.
5   Z. Liu, A. D. Koffman, B. C. Waltrip, and Y. Wang: J. Res. Natl. Inst. Stand. Technol. **118** (2013) 140.
6   Z. Liu, W. Li, F. Xue, J. Xiafang, B. Bu, and Y. Zheng: IEEE Trans. Magn. **51** (2015) 6201907.
7   P. Gao, C. Wang, Y. Zhi, and Y. Li: Nondestr. Test. Eval. **29** (2014) 229.
8   T. Bouchala, B. Abdelhadi, and A. Benoudjit: Nondestr. Test. Eval. **30** (2015) 1.
9   B. F. Yang, H. Zhang, C. Zhang, and Z. B. Zhang: Nondestr. Test. Eval. **28** (2013) 354.
10   W. Yin, G. Chen, L. Chen, and B. Wang: IEEE Sens. J. **11** (2011) 2233.
11   J. M. Masciotti, J. M. Lasker, and A. H. Hielscher: IEEE Trans. Instrum. Meas. **57** (2008) 182.
12   Y. Li, Z. Liu, W. Yuan, Y. Yue, and Z. L. Liu: IEEE I2MTC (2020).
13   X. Ma, A. J. Peyton, S. R. Higson, A. Lyons, and S. J. Dickinson: Meas. Sci. Technol. **17** (2006) 111.
14   J. W. Huo, Z. Liu, C. F. Wang, and Z. L. Liu: 2019 PIERS - Spring IEEE (2019) 19430009.